PAPER IN FOREFRONT

Highly efficient preconcentration using anodically generated shrinking gas bubbles for per- and polyfluoroalkyl substances (PFAS) detection

Ruchiranga Ranaweera[1] · Shizhong An[2] · Yue Cao[1] · Long Luo[1] ⓘ

Abstract

Here we report a highly efficient PFAS preconcentration method that uses anodically generated shrinking gas bubbles to preconcentrate PFAS via aerosol formation, achieving ~ 1400-fold enrichment of PFOS and PFOA—the two most common PFAS—in 20 min. This new method improves the enrichment factor by 15 to 105% relative to the previous method that uses cathodically generated H_2 bubbles. The shrinking gas bubbles are in situ electrogenerated by oxidizing water in an NH_4HCO_3 solution. H^+ produced by water oxidation reacts with HCO_3^- to generate CO_2 gas, forming gas bubbles containing a mixture of O_2 and CO_2. Due to the high solubility of CO_2 in aqueous solutions, the CO_2/O_2 bubbles start shrinking when they leave the electrode surface region. A mechanistic study reveals two reasons for the improvement: (1) shrinking bubbles increase the enrichment rate, and (2) the attractive interactions between the positively charged anode and negatively charged PFAS provide high enrichment at zero bubble path length. Based on this preconcentration method, we demonstrate the detection of ≥ 70 ng/L PFOA and PFOS in water in ~ 20 min by coupling it with our bubble-nucleation-based detection method, fulfilling the need of the US Environmental Protection Agency.

Keywords Bubble bursting aerosol · Preconcentration · PFAS detection · Electrochemistry

Introduction

Per- and polyfluoroalkyl substances (PFAS) are a group of emerging contaminants ubiquitously present in the environment because of their wide use in firefighting foam, stain repellents, nonstick coatings, cleaning products, and electroplating [1]. Due to their strong C-F bonds, PFAS are highly stable and environmentally persistent, leading to bioaccumulation in humans and causing health problems, such as

prostate and kidney cancer, thyroid disease, and cardiovascular disease [2]. As a result, the US Environmental Protection Agency (EPA) published a health advisory in 2016 for perfluorooctane sulfonate (PFOS) and perfluorooctanoic acid (PFOA)—the two most common PFAS—in drinking water to be 70 ng/L individually or combined [3]. In 2018, the US EPA further identified addressing the PFAS problem as one of the national priorities [4], motivating research on PFAS detection and remediation.

The US EPA Method 537 is currently the standard analytical method for detecting PFAS in drinking water [5]. This method comprises a multi-step preconcentration procedure using solid-phase extraction and a separation and detection procedure using liquid chromatography/tandem mass spectrometry (LC/MS/MS) [5]. Special equipment and specially trained personnel are necessary to perform this test, making it expensive (~ $300 per sample) and time-consuming. The typical laboratory turnaround time is > 2 weeks, so real-time monitoring of PFAS contamination is challenging, limiting our ability to respond to PFAS outbreaks rapidly.[6]

In recent years, much effort has been devoted to developing low-cost and rapid alternative methods for PFAS

✉ Long Luo
long.luo@wayne.edu

[1] Department of Chemistry, Wayne State University, Detroit, MI 48202, USA

[2] School of Materials Science and Engineering, Henan University of Science and Technology, Luoyang 471023, China

detection to address the limitations of the standard method [6]. One popular PFAS sensor design involves using molecularly imprinted polymers (MIPs) as the recognition element. MIPs with an affinity for PFAS are prepared by initiating polymerization of monomers in the presence of the targeted PFAS molecule that is extracted afterward, leaving behind the cavities in the polymer matrix complementary to the chosen PFAS molecule. These MIPs were applied to various sensing platforms to build PFAS sensors, including potentiometric [7], voltammetric [8–10], fluorometric [11, 12], and photoelectrochemical [13]. A few MIP-based PFAS sensors were reported to detect PFAS with concentrations lower than the EPA health advisory limit of 70 ng/L, but their specificity for PFAS is often not ideal because common species in water such as chloride ions and humic acid can produce false-positive signals [9]. The antibodies against PFOA developed by Cennamo et al. [14] may potentially provide better specificity for PFAS than the MIPs, but the detection limit of the antibody-based PFAS sensor currently does not meet the EPA requirement.

To address the insufficient limit of detection (LOD) for most existing PFAS sensors, we previously developed a PFAS preconcentration method based on electrochemical aerosol formation [14], which exhibits ~1000-fold preconcentration of ten common PFAS in the concentration range from 1 pM to 1 nM (or ~0.5 to 500 ng/L) in 10 min. This preconcentration method relies on the spontaneous adsorption of PFAS onto the surface of electrogenerated H_2 gas bubbles and the subsequent formation of aerosol droplets during the bubble bursting at the solution/air interface (Fig. 1a). These aerosol droplets are enriched with PFAS because when a bubble bursts, only a thin layer of liquid around a gas bubble is ejected into the air, converting the high surface concentration of PFAS at the gas/liquid interface of gas bubbles to a high bulk concentration in the aerosol droplets [15–19].

Here, we present an improved PFAS preconcentration method using anodically generated shrinking gas bubbles, increasing PFAS enrichment factor by 15 to 105% relative to the previous cathodic method. Based on this new, highly efficient preconcentration method, we demonstrate the detection of 70 ng/L PFOA and PFOS in water in ~20 min by coupling it with a bubble-nucleation-based detection method developed by our laboratory.

Experimental section

Chemicals and materials

Perchloric acid ($HClO_4$, 70%), sodium perchlorate ($NaClO_4$, 98%), perfluorooctanoic acid (PFOA), undecaflurohexanoic acid (PFHxA), perfluoroheptanoic acid (PFHpA),
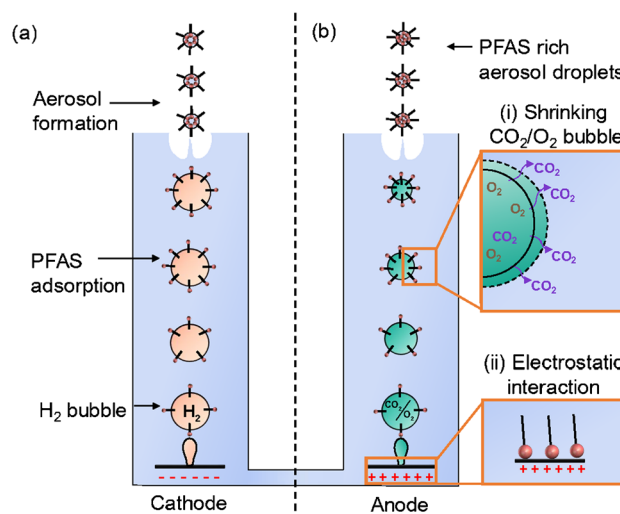

Fig. 1 Preconcentration of PFAS via electrochemical aerosol formation using (**a**) cathodically generated H_2 bubbles and (**b**) anodically generated CO_2/O_2 gas bubbles. Because of the high solubility of CO_2 in water, the CO_2/O_2 gas bubbles shrink as they float upward. The preconcentration efficiency is improved due to the bubble size reduction and electrostatic interaction between oppositely charged PFAS and anode

perfluorononanoic acid (PFNA), perfluorodecanoic acid (PFDA), tridecafluorohexane-1-sulfonic acid (PFHxS), heptadecafluorooctanesulfonic acid (PFOS), ammonium bicarbonate, sodium phosphate monobasic, and sodium phosphate dibasic were purchased from Sigma-Aldrich. Perfluoroheptanesulfonic acid (PFHpS) was purchased from Synquest Laboratories.

Electrochemical aerosol enrichment

Home-built H-type polypropylene two-compartment electrochemical cell was used in all the aerosol enrichment experiments. The cell has a total volume of ~650 mL. All the electrolyte solutions had a concentration of 0.2 M, and 1.5 cm × 1.5 cm Ni foam electrodes were separately immersed in the two compartments as the anode and cathode. A constant current of 0.2 A was applied between the two electrodes to generate microsized gas bubbles by water electrolysis. A 50 μL of bursting bubble aerosol was collected from the anodic compartment and cathodic compartment separately using a glass slide placed at ~3 mm above the liquid surface and then transferred to 600-μL polypropylene autosampler vials.

Bubble size distribution analysis

Photographs of gas bubbles in anode and cathode at different heights were taken using a Sony alpha a7 II full-frame Mirrorless camera with Venus Optics Laowa 24 mm f/14

probe lens (manual mode, aperture f40, ISO 1600, shutter speed 1/1600 s). All the images were analyzed using ImageJ software (NIH, Bethesda, MD).

Electrochemical measurements

All experiments were carried out using a CHI 760E potentiostat and inside a well-grounded Faraday cage. An Ag wire was used as the counter/reference electrode during the bubble-nucleation-based measurements. Note that any counter electrodes should work in the bubble-nucleation-based measurements because the peak current associated with bubble nucleation is the readout, and the electrode potential is not important.

Nanoelectrode fabrication method

Nanoelectrodes were fabricated following the procedures in the literature [20]. A 4 N pure 1 cm long and 25 µm in diameter polycrystalline Pt wire (Surepure Chemetals) was attached to a W rod using Ag conductive epoxy (M.G. Chemicals). The end of the Pt wire was electrochemically etched in a 15 wt% $CaCl_2$ solution to make a sharp nanotip. A sharpened wire was then inserted into a glass capillary (Dagan Corporation, o.d./i.d., 1.65/1.10 mm, softening point 712 °C) and thermally sealed using H_2/O_2 flame. Then the sealed tip was polished using successively finer silicon carbide polishing sandpapers (Buehler with grid sizes of 600 and 1200) until the Pt nanodisk was exposed, which was monitored using electronic feedback circuit. The radius of the nanodisk electrodes, r, was determined by the diffusion-limited current for proton reduction (i_d) in 0.10 M $HClO_4$ solution containing 0.10 M $NaClO_4$. The radius was calculated using the following equation $i_d = 4FDCr$. D is the diffusion coefficient of H^+, and C is the bulk concentration of $HClO_4$. The literature value of $D = 7.8 \times 10^{-5}$ cm^2/s for H^+ was used to compute r.

PFAS analysis

Collected aerosol samples were diluted 50 times by 50:50 v:v H_2O/MeOH before LC/MS/MS analysis using a Nexera-X2 ultra-performance liquid chromatography with a Shimadzu 8040 triple quadrupole mass analyzer operated in negative ionization and multiple reaction monitoring (MRM) modes. Fifty microliters of aliquots of sample extracts was injected onto an analytical column (Accucore™ C8 column 2.1 × 100 mm, 2.6 µm; Thermo Fisher Scientific). A gradient of 20 mM ammonium acetate in water (solvent A) and 100% acetonitrile (solvent B) was used for the elution procedure as follows: 0–1 min, 5% B; 1–2 min, 5 to 30% B; 2–11 min, 30 to 57% B; 11–12 min, 57 to 98% B; 12–13 min, 98% B; 13–14 min, 98 to 5% B. The flow rate was 0.4 mL min^{-1}, and the temperature of the analytical column was maintained at

30 °C. The nebulizing gas flow was kept at 3 L/min, and the drying gas flow was 15 L/min.

Surface tension measurements

Surface tension measurements were performed using a Kruss BP100 bubble-pressure tensiometer (Kruss GmbH, Germany). The surface tension data were collected at the surface age of 100 s when the surface tension reached equilibrium. The capillary diameter was 0.228 mm when taking the bubble pressure measurements.

Results and discussion

Preconcentration method design

There are two essential processes during aerosol preconcentration: (i) the spontaneous adsorption of PFAS from the bulk solution onto the bubble surface and (ii) the formation of PFAS-enriched aerosol droplets when a bubble bursts. Our previous study found that the gas bubble radius (r_{bubble}) played a critical role in both processes [14]. For spontaneous adsorption, because of the spherical diffusion field around a gas bubble, the diffusion flux of PFAS from the surrounding solution to the bubble surface is inversely proportional to r_{bubble}. For aerosol formation, according to the empirical rule [21], the ratio of aerosol droplet size ($r_{aerosol}$) to r_{bubble} is a constant of ~ 10%. Thus, the conversion from the surface concentration on gas bubbles ($C_{PFAS, bubble}$) to the PFAS concentration in the aerosol droplets ($C_{PFAS, aerosol}$) is also r_{bubble}-dependent. Taking both effects together, we previously derived the following expression for the enrichment rate of electrochemical aerosol preconcentration [14]:

$$\frac{\partial R}{\partial h} = a \frac{D_{PFAS}}{r_{bubble}^4} \tag{1}$$

where R is the enrichment factor defined as the ratio of $C_{PFAS,aerosol}$ to the PFAS concentration in the sample solution ($C_{PFAS, bulk}$), h is the path length that gas bubbles travel, D_{PFAS} is the diffusion coefficient of PFAS in water, and a is a constant of 2.4×10^{-4} m^2/s. Inspired by Eq. 1, we hypothesize that shrinking gas bubbles would improve the aerosol preconcentration efficiency because of the negative correlation between enrichment rate ($\frac{\partial R}{\partial h}$) and r_{bubble}.

The shrinking gas bubbles are in situ electrogenerated by oxidizing water in 0.20 M NH_4HCO_3. One equivalent of H_2O produces 0.5 equivalent of O_2 gas and 2 equivalents of H^+ (Eq. 2). The latter reacts with HCO_3^- to generate 2 equivalents of CO_2 gas (Eq. 3), forming gas bubbles containing a mixture of O_2 and CO_2 with a molar ratio of 0.5:2.
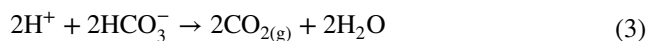
$$H_2O - 2e \rightarrow 2H^+ + \frac{1}{2}O_{2(g)} \qquad (2)$$

$$2H^+ + 2HCO_3^- \rightarrow 2CO_{2(g)} + 2H_2O \qquad (3)$$

Due to the high solubility of CO_2 in aqueous solutions, the CO_2/O_2 bubbles start shrinking when they leave the CO_2-saturated electrode surface region and float upward into the CO_2-free bulk solution (Fig. 1b). In addition, because the CO_2/O_2 bubbles are generated at the anode, we hypothesize that the attractive interactions between the positively charged anode and negatively charged PFAS would improve the pre-concentration efficiency.

Preconcentration of PFAS

Preconcentration experiments were carried out using a similar experimental setup as our previous work (see Electronic Supplementary Material Fig. S1) [14]. Briefly, a constant current of 0.2 A was applied between two 1.5 cm^2 Ni foam electrodes separately immersed at a depth of 25 cm in the two compartments of a home-built polypropylene H-type cell. The sample is a 650 mL 0.2 M NH_4HCO_3 solution containing low levels of PFAS (pH = 8.4). A microscope slide was placed at ~3 mm above the liquid surface of each compartment to collect the aerosol droplets enriched with PFAS for 20 min (see Electronic Supplementary Material Fig. S2). The collection rates of aerosol droplets were ~11 µL/min from the cathode side and ~7 µL/min from the anode side. Before being introduced to LC/MS/MS for PFAS quantification, the collected aerosol samples were diluted by 50 times using a 50/50 v/v H_2O and MeOH mixture. The information on the ion peaks and calibration curves used for PFAS LC/MS/MS quantitation is provided in Electronic Supplementary Material Fig. S3 and Table S1. In the initial experiments, we observed substantial variations in the enrichment factor on the anodic side when employing freshly cut Ni foam electrodes due to the structural and compositional evolution of the Ni electrode to $NiO(OH)_x$ under water oxidation conditions, as evidenced by the significant electrode potential drift, causing unstable bubble generation (see Electronic Supplementary Material Fig. S4). The irreproducibility problem was solved by aging the Ni anode in 0.2 M NH_4HCO_3 under a constant current of 0.2 A for ~20 min before use. After 20 min, a steady stream of uniform bubbles was observed, indicating a stabilized electrode structure (see Electronic Supplementary Material Fig. S4). Furthermore, we analyzed the morphology and chemical composition of the Ni electrode before and after the electrochemical conditioning using scanning electron microscopy (SEM) and X-ray photoelectron spectroscopy (XPS). SEM images do not show any significant morphology change (see Electronic Supplementary Material Fig. S5), but the XPS data shows

the formation of $Ni(OH)_2$ and NiO on both Ni cathode and anode during the electrochemical conditioning (see Electronic Supplementary Material Fig. S6 and Table S2).

Figure 2a shows the R-values for eight PFAS compounds, including five perfluoroalkyl carboxylates with carbon chain lengths from 6 to 10 (undecafluorohexanoic acid (PFHxA), perfluoroheptanoic acid (PFHpA), perfluorooctanoic acid (PFOA), perfluorononanoic acid (PFNA), and perfluoro-decanoic acid (PFDA)) and three perfluoroalkyl sulfonates with carbon chain from 6 to 8 (tridecafluorohexane-1-sulfonic acid (PFHxS), perfluoroheptanesulfonic acid (PFHpS), and heptadecafluorooctanesulfonic acid (PFOS)) at $C_{PFAS, bulk} = 50$ ng/L using anodic and cathodic aerosol preconcentration. For all PFAS, anodic aerosol preconcentration produced higher R-values than the cathodic ones, with an average improvement of ~30%, indicating the success of our new preconcentration method design. Note in these experiments that the PFAS concentration is too low to cause any noticeable equilibrium surface tension changes (see Electronic Supplementary Material Fig. S7), so the different R-values observed among PFAS compounds should be caused by their different adsorption behaviors onto the bubble surface and their effects on bubble bursting behaviors. Furthermore, the increased preconcentration efficiency was observed over an extensive concentration range, for instance, from 10^{-11} M to 10^{-7} M (~4 ng/L to 14 µg/L) for PFOA (Fig. 2b). The anodic aerosol preconcentration was also tested for enriching a mixture of PFOA, PFNA, PFHxA, and PFHxS to assess the potential interferences between PFAS compounds. Impressively, we did not observe any apparent differences between the R-values obtained from this mixture preconcentration experiment (red bars in Fig. 1c) and the reference values obtained from the preconcentration of individual compounds (green bars in Fig. 1c).

Mechanism understanding

As introduced in the method design, we hypothesized that (1) shrinking bubbles would improve the aerosol preconcentration efficiency because of the negative correlation between the enrichment rate and bubble size and (2) the attractive interactions between the positively charged anode and negatively charged PFAS would further improve the pre-concentration efficiency.

To test our hypothesis, we first measured the bubble size in the electrolytic cell. Fig. 3a and b show the photographs and size distributions of gas bubbles at various vertical distances from the electrode surface (or h) in the anodic and cathodic compartments. On the anodic side, r_{bubble} is initially 84 ± 12 µm near the anode ($h = 2.5$ cm) and decreases as the bubbles float upward and away from the anode and eventually becomes 42 ± 3 µm at $h = 20$ cm, corresponding to a total volume reduction of 87.5%. This

Fig. 2 **a** Enrichment factor, R, for five perfluorinated carboxylic acids with carbon chain lengths from 6 to 10 (PFHxA, PFHpA, PFOA, PFNA, and PFDA) and three perfluorinated sulfonic acids with carbon chain lengths from 6 to 8 (PFHxS, PFHpS, and PFOS) using the anodic and cathodic aerosol formation. The initial PFAS concentrations ($C_{PFAS, bulk}$) were 50 ng/L for all experiments. **b** The plot of R vs. $C_{PFOA, bulk}$. **c** Preconcentration of a mixture of PFOA, PFNA, PFHxA, and PFHxS using anodic preconcentration. For each PFAS compound, $C_{PFAS, bulk} = 50$ ng/L. The reference R-values were from the experiments in (**a**). The error bars are the standard deviations of three independently collected data points in each plot
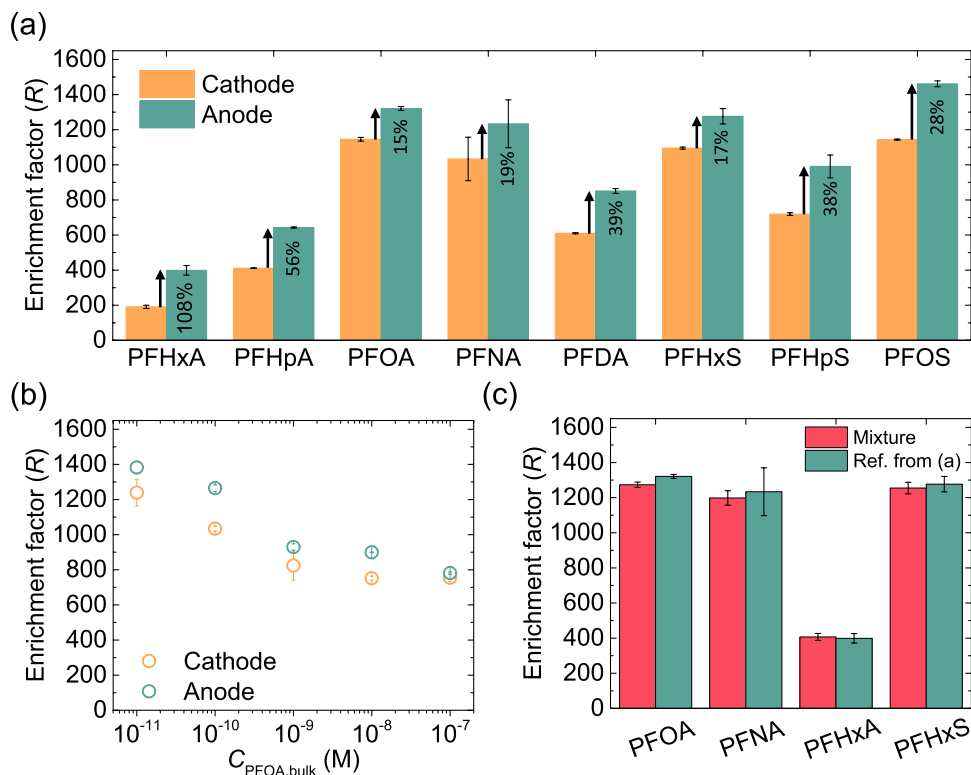
percent volume change is comparable to the theoretical value of 80% in the case of the complete dissolution of CO_2 from the CO_2/O_2 gas bubbles. In contrast, gas bubbles on the cathodic side show no noticeable change in radius: 73 ± 9 μm at $h = 2.5$ cm vs. 73 ± 10 μm at $h = 20$ cm. Such difference results from the much higher solubility of CO_2 in water (~ 39 mM) [22] than H_2 (~ 0.8 mM) [23]. As a control, we also performed size analysis in a phosphate buffer electrolyte solution, where only O_2 and H_2 bubbles were produced. We found that O_2 and H_2 bubble sizes only slightly ($< 15\%$) decreased from 65 ± 11 μm at $h = 2.5$ cm to 56 ± 11 μm at $h = 20$ cm and from 69 ± 12 μm to 60 ± 8 μm, respectively (Fig. 3c, d). Figure 4a and b summarize the average r_{bubble} as a function of h in NH_4HCO_3 and phosphate buffer solutions, respectively.

Next, we measured the R-values achieved at various h. In both NH_4HCO_3 and phosphate buffer solutions, the anodic side yields higher enrichment than the cathodic side (Fig. 4c, d). When NH_4HCO_3 is used, the enrichment rate (i.e., the slope of the R-h plot) at the anodic side is $\sim 26\%$ larger than that at the cathodic side (49 cm^{-1} vs. 39 cm^{-1}), whereas the enrichment rate is nearly identical in the two compartments for phosphate buffer (31 cm^{-1} vs. 29 cm^{-1}). This finding confirms our first hypothesis that shrinking bubbles improve aerosol preconcentration efficiency by increasing the enrichment rate. However, the improvement over the enrichment rate does not follow the fourth-order dependence on $1/r_{bubble}$ as described in Eq. 1, possibly because the steady-state

diffusion assumption used in the derivation of Eq. 1 [14] is not valid in this dynamic shrinking bubble system.

Figure 4c and d also show that the enrichment factor at zero bubble path significantly contributes to the improved enrichment factor on the anodic side over the cathodic one ($R = \sim 400$ for anode vs. ~ 200 for cathode at $h = 0$). The enrichment at $h = 0$ arises from two interfaces: the electrode/solution interface and the solution/air interface. For the electrode/solution interface, Lipkowski, Burgess, and other groups [24–31] have comprehensively investigated the potential-driven adsorption and aggregation of anionic, zwitterionic, and cationic surfactants on metal electrodes surfaces. They found that anionic surfactants such as sodium dodecyl sulfate (SDS) would undergo a phase transition from long-range ordered hemicylindrical hemimicelles to a disordered bilayer as the electrode potential becomes positive, doubling the SDS concentration at the electrode/solution interface [25, 32]. In contrast, for cationic surfactants such as cetrimonium bromide (CTAB), they found that the amount of CTAB at the interface decreased at a highly positive charged electrode surface. However, the amount of interfacial CTAB did not fall to zero because the opposite charge from the co-adsorbed bromide ions serves to mitigate repulsive electrostatic forces between the electrode and CTAB, which would otherwise make ammonium adsorption unfavorable at positive electrode polarization [24]. Inspired by these previous findings, we performed the following experiment to confirm that the observed different enrichment
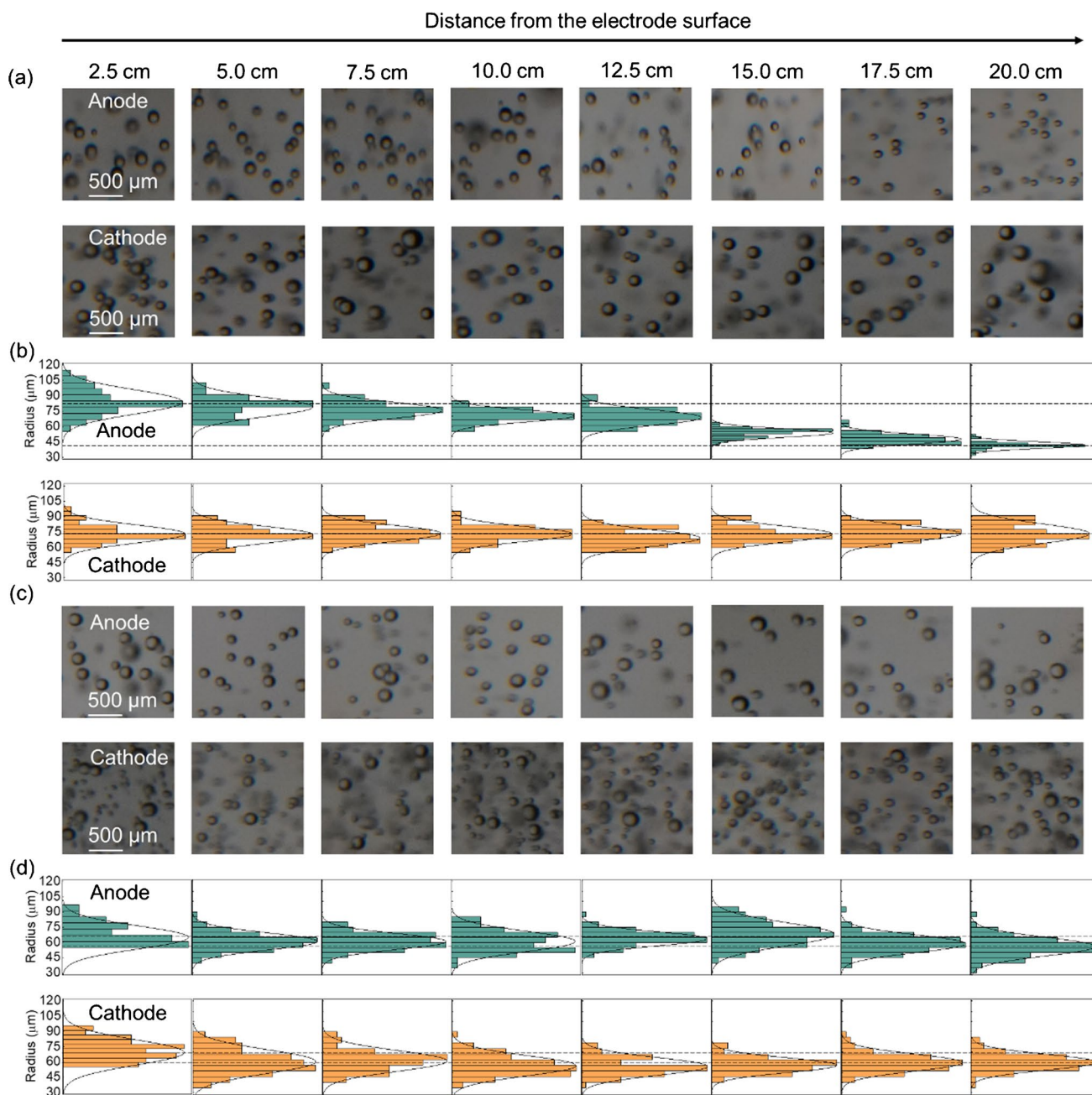
Fig. 3 Photographs of gas bubbles at different h in anodic and cathodic compartments using (**a**) 0.2 M NH_4HCO_3 (pH = 8.4) and (**c**) 0.2 M phosphate buffer (pH = 7) as the electrolyte solution. (**b**), (**d**) The corresponding distributions of bubble radii (r_{bubble}) as a function of h. Each distribution profile was obtained by analyzing 100 bubbles. The current was held at a constant value of 0.2 A

factors at $h = 0$ between anodic and cathodic sides are indeed caused by the electrostatic interactions between PFOA and electrode surface, utilizing the different potential-driven adsorption and aggregation behaviors of anionic and cationic surfactants on an electrode surface. Specifically, we carried out the preconcentration experiment for 50 ng/L CTAB. We found the enrichment factor for CTAB was ~ 30% higher on the cathodic side than the anodic one in both NH_4HCO_3 and phosphate buffer solutions (Fig. 5), exactly opposite to

PFOA's, confirming our second hypothesis that the electrostatic interactions between the positively charged anode and negatively charged PFAS further improve the preconcentration efficiency.

Detection of 70 ng/L PFOA and PFOS

Our laboratory has previously reported a bubble-nucleation-based electrochemical detection (BED) method for

Fig. 4 **a**, **b** Plots of r_{bubble} as a function of h in the anodic and cathodic compartments for 0.2 M NH$_4$HCO$_3$ and 0.2 M phosphate buffer. **c**, **d** Plots of R vs. h. The initial PFOA concentration in the solution is 50 ng/L
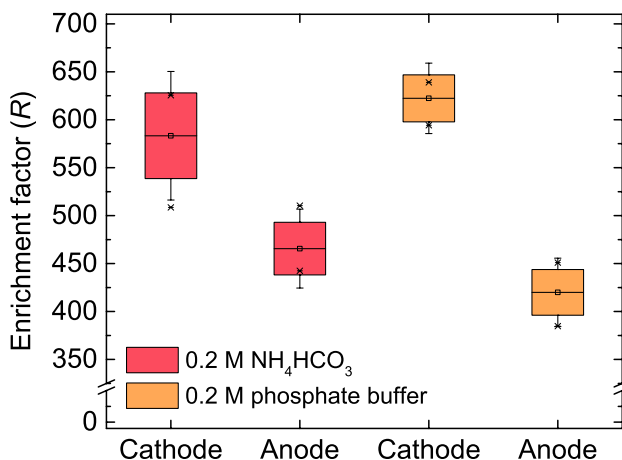

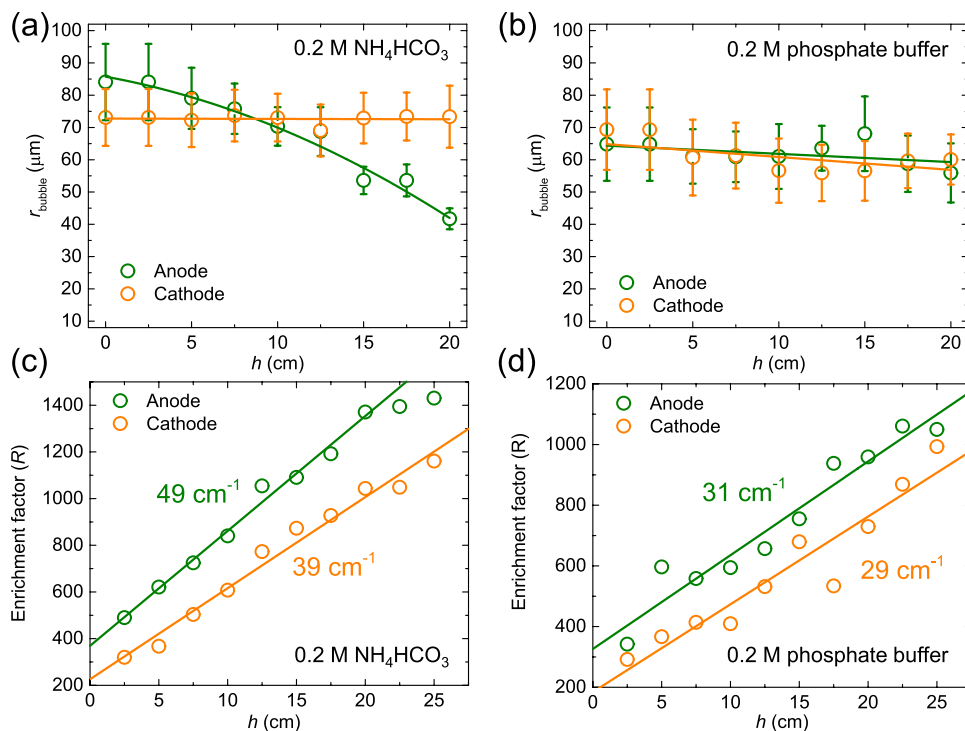**Fig. 5** Box plots of the enrichment factor for a cationic surfactant, cetrimonium bromide (CTAB), at $C_{CTAB, bulk} = 50$ ng/L in (**a**) 0.2 M NH$_4$HCO$_3$ and (**b**) 0.2 M phosphate buffer on the anodic and cathodic sides. Ni foam electrodes were immersed at a fixed depth of 25 cm, and a constant current of 0.2 A was applied

PFAS detection [33]. The BED method utilizes the high surface activity of PFAS to influence the electrochemical bubble nucleation and then transduces the change in nucleation condition to an electrochemical signal for determining the PFAS concentration. The BED method mainly responds to PFAS with 7- and 8-carbon chain length (including PFOS, PFOA, PFHpS, and PFHpA) due to the high surface activity of these four compounds. The senstivity of the BED method for PFOS and PFOA is similar and about one order of magnitude higher than PFHpS and PFHpA, making it suitable for screening PFOA and PFOS in water. However, its LOD for PFOS and PFOA is merely ~ 80 µg/L and 30 µg/L, respectively, which does not satisfy the target LOD of 70 ng/L set by the US EPA. Thus, a preconcentration step is necessary. As shown in Fig. 2a, an enrichment factor of ~ 1400 was achieved using anodically generated shrinking gas bubbles for PFOA and PFOS. Therefore, after adding this electrochemical aerosol preconcentration step, the target LOD of 70 ng/L should be achievable.

To test its feasibility, we first preconcentrated PFOA and PFOS from 70 ng/L PFOS and PFOA solutions for 20 min, respectively. The collected PFAS-enriched aerosol droplets were acidified with 1 M HClO$_4$ containing 0.1 M NaClO$_4$, which is necessary for BED measurements. During the acidification, the PFAS samples were diluted by a factor of 2. Then, we performed the BED measurements using these samples (the photograph of the setup and the raw cyclic voltammograms are provided in Electronic Supplementary Material Fig. S8). Figure 6a plots the bubble nucleation currents (i_{peak}) for aerosol samples collected from the anodic and cathodic compartments after being normalized by the nucleation current of the blank without PFOA or PFOS (i_{peak}^0). According to the one-tailed two-sample t-test results, all four PFAS-enriched aerosol samples are statistically
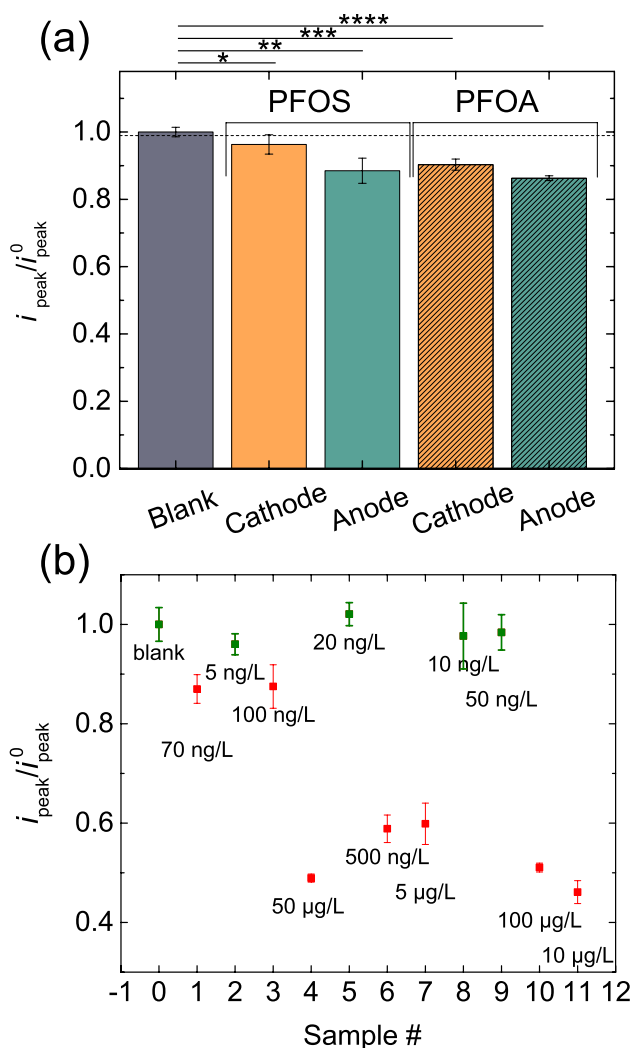
Fig. 6 **a** Normalized electrochemical bubble nucleation currents (i_{peak}/i_{peak}^0) for blank and the PFAS-enriched aerosol samples collected from 70 ng/L PFOS and PFOA solutions in the anodic and cathodic compartments. (one-tailed two-sample *t*-test, $t=1.94$, $df=6$; i_{peak} vs. i_{peak}^0, *$p<0.03$, ** $p<0.001$, *** $p<2\times10^{-5}$, **** $p<1\times10^{-6}$.) **b** i_{peak}/i_{peak}^0 for PFOA-enriched aerosol samples collected from 11 different PFOA-containing samples with concentrations ranging from 5 ng/L to 100 µg/L in a blind test. The aerosol samples were collected from the anodic compartments at $h=25$ cm. The samples highlighted in red are statistically different from the blank according to the one-tailed two-sample *t*-test at a confidence interval of 95%. The error bars are the standard deviations from four independent BED measurements

different from the blank at a confidence interval of 95% ($p<0.05$). For the two samples collected from the anodic side, the confidence level is higher than 99%.

Next, we performed a blind test for 11 PFOA samples with concentrations ranging from 5 ng/L to 100 µg/L. Similarly, the electrochemical aerosol preconcentration was carried out using these unknown PFOA samples. This time, only the aerosol samples collected from the

anodic side were subject to the BED measurements. The raw cyclic voltammograms are provided in Electronic Supplementary Material Fig. S9. Figure 6b summarizes the normalized i_{peak} for all samples. Excitingly, only the samples with PFOA concentrations higher or equal to 70 ng/L were found to be statistically different from the blank according to the one-tailed two-sample *t*-test at a confidence interval of 95%, which is consistent with the expected LOD of ~ 42 ng/L calculated from the native LOD of the BED method (30 µg/L for PFOA), the enrichment factor of ~ 1400, and a dilution factor of 2. Furthermore, we tested our method using tap water and bottled water samples. In both cases, we successfully detected the presence of 70 ng/L PFOA spiked in the samples (see Electronic Supplementary Material Fig. S10). The successful detection of ≥ 70 ng/L PFOA in a blind test and real-world water samples suggests the potential practical use of our bubble-based preconcentration and detection methods for screening PFAS in drinking water.

Conclusion

In conclusion, we present an improved PFAS preconcentration method using anodically generated shrinking gas bubbles, increasing PFAS enrichment factor by 15 to 105% relative to the previous cathodic method. A mechanistic study reveals two reasons for the improvement: (1) shrinking bubbles increase the enrichment rate, and (2) the attractive interactions between the positively charged anode and negatively charged PFAS provide high enrichment at zero bubble path length. Based on this new, highly efficient preconcentration method, we demonstrate the detection of ≥ 70 ng/L PFOA and PFOS in water in ~ 20 min by coupling it with our bubble-nucleation-based detection method. After meeting the desired limit of detection for PFAS, we are currently working on addressing the limited specificity of the aerosol-based preconcentration and BED detection methods utilizing the high chemical stability of PFAS over non-PFAS surfactant interferences.

Declarations

Conflict of interest The authors declare no competing interests.

References

1. Glüge J, Scheringer M, Cousins IT, DeWitt JC, Goldenman G, Herzke D, et al. An overview of the uses of per- and poly-fluoroalkyl substances (PFAS). Environ Sci: Process Impacts. 2020;22(12):2345–73.
2. Sunderland EM, Hu XC, Dassuncao C, Tokranov AK, Wagner CC, Allen JG. A review of the pathways of human exposure to poly- and perfluoroalkyl substances (PFASs) and present understanding of health effects. J Expo Sci Environ Epidemiol. 2019;29(2):131–47.
3. U. S. Environmental Protection Agency. Drinking water health advisories for PFOA and PFOS 2016. Available from: https://www.epa.gov/ground-water-and-drinking-water/drinking-water-health-advisories-pfoa-and-pfos. Accessed 26 Feb 2019.
4. U. S. Environmental Protection Agency. National priorities: per- and polyfluoroalkyl substances 2018. Available from: https://www.epa.gov/research-grants/national-priorities-and-polyfluoroalkyl-substances. Accessed 26 Feb 2019.
5. Shoemaker J, Grimmett P, Boutin B. Method 537. Determination of selected perfluorinated alkyl acids in drinking water by solid phase extraction and liquid chromatography/tandem mass spectrometry (LC/MS/MS) U. S. Environmental Protection Agency: Cincinnati, OH2009. Available from: https://www.epa.gov/water-research/epa-drinking-water-research-methods. Accessed 26 Feb 2019.
6. Al Amin M, Sobhani Z, Liu Y, Dharmaraja R, Chadalavada S, Naidu R, et al. Recent advances in the analysis of per- and polyfluoroalkyl substances (PFAS)—a review. Environ Technol Innov. 2020;19:100879.
7. Fang C, Chen Z, Megharaj M, Naidu R. Potentiometric detection of AFFFs based on MIP. Environ Technol Innov. 2016;5:52–9.
8. Glasscott MW, Vannoy KJ, Kazemi R, Verber MD, Dick JE. μ-MIP: molecularly imprinted polymer-modified microelectrodes for the ultrasensitive quantification of GenX (HFPO-DA) in river water. Environ Sci Technol Lett. 2020;7(7):489–95.
9. Kazemi R, Potts EI, Dick JE. Quantifying interferent effects on molecularly imprinted polymer sensors for per- and polyfluoroalkyl substances (PFAS). Anal Chem. 2020;92(15):10597–605.
10. Karimian N, Stortini AM, Moretto LM, Costantino C, Bogialli S, Ugo P. Electrochemosensor for trace analysis of perfluorooctanesulfonate in water based on a molecularly imprinted poly(o-phenylenediamine) polymer. ACS Sens. 2018;3(7):1291–8.
11. Liu Q, Huang A, Wang N, Zheng G, Zhu L. Rapid fluorometric determination of perfluorooctanoic acid by its quenching effect on the fluorescence of quantum dots. J Lumin. 2015;161:374–81.
12. Feng H, Wang N, Tran TT, Yuan L, Li J, Cai Q. Surface molecular imprinting on dye–(NH2)–SiO2 NPs for specific recognition and direct fluorescent quantification of perfluorooctane sulfonate. Sens Actuators B Chem. 2014;195:266–73.
13. Tran.T T, Li J, Feng H, Cai J, Yuan L, Wang N, et al. Molecularly imprinted polymer modified TiO2 nanotube arrays for photoelectrochemical determination of perfluorooctane sulfonate (PFOS). Sens Actuators B Chem. 2014;190:745–751.
14. Cao Y, Lee C, Davis ETJ, Si W, Wang F, Trimpin S, et al. 1000-fold preconcentration of per- and polyfluorinated alkyl substances within 10 minutes via electrochemical aerosol formation. Anal Chem. 2019;91(22):14352–8.
15. Chingin K, Cai Y, Chagovets V, Kononikhin A, Starodubtseva N, Frankevich V, et al. Preconcentration of organic solutes in urine by bubble bursting. Metabolomics. 2016;12(11):171.
16. Chingin K, Cai Y, Liang J, Chen H. Simultaneous preconcentration and desalting of organic solutes in aqueous solutions by bubble bursting. Anal Chem. 2016;88(10):5033–6.
17. Chingin K, Yan R, Zhong D, Chen H. Enrichment of surface-active compounds in bursting bubble aerosols. ACS Omega. 2018;3(8):8709–17.
18. Lee C, Yang T-L, Yao Y-Z, Li J-Y, Huang C-L. Rapid detection of perfluorinated sulfonic acids through preconcentration by bubble bursting and surface-assisted laser desorption/ionization. J Mass Spectrom. 2021;56(4): e4667.
19. An S, Ranaweera R, Luo L. Harnessing bubble behaviors for developing new analytical strategies. Analyst. 2020;145:7782–7795.
20. Zhang B, Galusha J, Shiozawa PG, Wang G, Bergren AJ, Jones RM, et al. Bench-top method for fabricating glass-sealed nanodisk electrodes, glass nanopore electrodes, and glass nanopore membranes of controlled size. Anal Chem. 2007;79(13):4778–87.
21. Kientzler CF, Arons AB, Blanchard DC, Woodcock AH. Photographic investigation of the projection of droplets by bubbles bursting at a water surface. Tellus. 1954;6(1):1–7.
22. Weiss RF. Carbon dioxide in water and seawater: the solubility of a non-ideal gas. Mar Chem. 1974;2(3):203–15.
23. Haynes WM. CRC Handbook of chemistry and physics. 95th ed. Hoboken: CRC Press; 2014.
24. Vivek JP, Burgess IJ. Quaternary ammonium bromide surfactant adsorption on low-index surfaces of gold. 2. Au(100) and the role of crystallographic-dependent adsorption in the formation of anisotropic nanoparticles. Langmuir. 2012;28(11):5040–5047.
25. Grossutti M, Leitch JJ, Seenath R, Karaskiewicz M, Lipkowski J. SEIRAS Studies of water structure in a sodium dodecyl sulfate film adsorbed at a gold electrode surface. Langmuir. 2015;31(15):4411–8.
26. Leitch JJ, Collins J, Friedrich AK, Stimming U, Dutcher JR, Lipkowski J. Infrared studies of the potential controlled adsorption of sodium dodecyl sulfate at the Au(111) electrode surface. Langmuir. 2012;28(5):2455–64.
27. Chen M, Burgess I, Lipkowski J. Potential controlled surface aggregation of surfactants at electrode surfaces–a molecular view. Surf Sci. 2009;603(10–12):1878–91.
28. Brosseau CL, Sheepwash E, Burgess IJ, Cholewa E, Roscoe SG, Lipkowski J. Adsorption of N-decyl-N, N, N-trimethylammonium triflate (DeTATf), a cationic surfactant, on the Au(111) electrode surface. Langmuir. 2007;23(4):1784–91.
29. Sek S, Chen M, Brosseau CL, Lipkowski J. In situ STM study of potential-driven transitions in the film of a cationic surfactant adsorbed on a Au(111) electrode surface. Langmuir. 2007;23(25):12529–34.
30. Burgess I, Zamlynny V, Szymanski G, Lipkowski J, Majewski J, Smith G, et al. Electrochemical and neutron reflectivity characterization of dodecyl sulfate adsorption and aggregation at the gold− water interface. Langmuir. 2001;17(11):3355–67.
31. Burgess I, Jeffrey C, Cai X, Szymanski G, Galus Z, Lipkowski J. Direct visualization of the potential-controlled transformation of hemimicellar aggregates of dodecyl sulfate into a condensed monolayer at the Au (111) electrode surface. Langmuir. 1999;15(8):2607–16.
32. Bickel KR, Timm AE, Nattland D, Schuster R. Microcalorimetric determination of the entropy change upon the electrochemically driven surface aggregation of dodecyl sulfate. Langmuir. 2014;30(30):9085–90.
33. Ranaweera R, Ghafari C, Luo L. Bubble-nucleation-based method for the selective and sensitive electrochemical detection of surfactants. Anal Chem. 2019;91(12):7744–8.

Ruchiranga Ranaweera is a fifth-year graduate student in the Department of Chemistry at Wayne State University, Detroit, MI, USA. His current research involves building electrochemical sensing platforms and extracting rare earth elements using electrochemically generated gas bubbles.

Yue Cao is an Assistant Professor in the department of materials science and engineering at Shandong University of Technology. His current research interests include electrogenerated bubbles, electrochemical sensors, and electrocatalytic materials.

Shizhong An is an Associate Professor in the School of Materials Science and Engineering at Henan University of Science and Technology, Luoyang, China. His current research interests are electrochemical, electrical, and magnetic materials.

Long Luo is the Carl R. Johnson Assistant Professor in the Department of Chemistry at Wayne State University, Detroit, MI, USA. His current research interests include electrogenerated bubbles, electrochemical synthesis of functional materials and molecules, and electrokinetic phenomena.